

# A semidiscrete finite volume formulation for multiprocess watershed simulation

Yizhong Qu<sup>1</sup> and Christopher J. Duffy<sup>1</sup>

Received 26 November 2006; revised 30 April 2007; accepted 9 May 2007; published 18 August 2007.

[1] Hydrological processes within the terrestrial water cycle operate over a wide range of time and space scales, and with governing equations that may be a mixture of ordinary differential equations (ODEs) and partial differential equations (PDEs). In this paper we propose a unified strategy for the formulation and solution of fully coupled process equations at the watershed and river basin scale. The strategy shows how a system of mixed equations can be locally reduced to ordinary differential equations using the semidiscrete finite volume method (FVM). Domain decomposition partitions the watershed surface onto an unstructured grid, and vertical projection of each element forms a finite volume on which all physical process equations are formed. The projected volume or prism is partitioned into surface and subsurface layers, leading to a fully coupled, local ODE system, referred to as the model “kernel.” The global ODE system is assembled by combining the local ODE system over the domain, and is then solved by a state-of-the-art ODE solver. The unstructured grid, based on Delaunay triangulation, is generated with constraints related to the river network, watershed boundary, elevation contours, vegetation, geology, etc. The underlying geometry and parameter fields are then projected onto the irregular network. The kernel-based formulation simplifies the process of adding or eliminating states, constitutive laws, or closure relations. The strategy is demonstrated for the Shale Hills experimental watershed in central Pennsylvania, and several phenomena are observed: (1) The enslaving principle is shown to be a useful approximation for soil moisture–water table dynamics for shallow soils in upland watersheds; (2) the coupling shows how antecedent moisture (i.e., initial conditions) can amplify peak flows; (3) the coupled equations predict the onset or threshold for upland ephemeral channel flow; and (4) the model shows how microtopographic information controls surface saturation and connectivity of overland flow paths for the Shale Hills site. The open-source code developed in this research is referred to as the Penn State Integrated Hydrologic Model (PIHM).

**Citation:** Qu, Y., and C. J. Duffy (2007), A semidiscrete finite volume formulation for multiprocess watershed simulation, *Water Resour. Res.*, 43, W08419, doi:10.1029/2006WR005752.

## 1. Introduction

[2] In this paper we address the problem of process integration for hydrologic prediction in watersheds and river basins. Simulation is now widely utilized as a complementary research methodology to theory and experiment [Post and Votta, 2005]. However, the grid resolution, scale of the model, and range of hydrologic processes operating in watersheds and river basins offer the dilemma of what is necessary to predict hydrologic response or to simulate certain behaviors of the coupled system. In this paper we formulate a multiscale strategy that incorporates constitutive relationships representing volume-average state variables. For small watersheds and fine numerical grids, local continuum relationships (e.g., Darcy’s law) lead to a fully coupled,

physics-based, distributed model. At larger scales and coarse grids, empirical relationships with large-scale volume averages are applied, and the model becomes a semidistributed model. A brief review of hydrologic modeling strategies demonstrates the issues involved with integration and coupling of multiple processes and clarifies the purpose of this paper.

[3] Current hydrologic models may be described from two perspectives: physically based, spatially distributed models, and lumped conceptual models. Freeze and Harlan [1969] developed the first blueprint for numerical solutions to physically based, distributed watershed models starting from a continuum perspective (i.e., Richards’ equations for subsurface flow, Saint Venant equations for surface flow and channel routing). It was some years before the SHE model [Abbott et al., 1986a, 1986b] and its variants produced a second generation where the coupled physical equations are actually solved on a regular grid, with coupling handled through a sophisticated control algorithm that passes information between processes (e.g., surface water–groundwater exchange).

<sup>1</sup>Department of Civil and Environmental Engineering, Pennsylvania State University, University Park, Pennsylvania, USA.

[4] The approach of coupling multiple processes through time-lagging and iterative coupling through boundary conditions is generally considered a weak form of coupling, in that it may lead to significant instability and errors [LaBolle *et al.*, 2003]. The approach also requires considerable reprogramming if changes are made to the physical equations for a specific application. More recently, Panday and Huyakorn [2004] have developed an approach where all equations in the model are of the diffusive type, which are solved in a single system on a regular grid (e.g., Richard's equation and diffusive wave equation), while equations for other processes (vegetation, energy, snow) are dealt with separately (iteratively). Yeh *et al.* [1998] have used a similar approach but with finite elements. As will be described later, our approach couples all dynamical equations within the same prismatic volume (a prism is defined by a triangle projected from the canopy, through the land surface to the lower boundary of groundwater flow); and all equations are solved simultaneously, eliminating the need for a controller, delayed, or off-line process equations.

[5] Lumped or spatially integrated models are widely used today, where the goal of the prediction is outflow from forcing (e.g., rainfall-runoff, recharge-baseflow, precipitation-infiltration). Lumped systems are low-dimensional and conveniently solved, but still require an empirical relationship for flux discharge that is generally assumed to be linear or weakly nonlinear and fitted or calibrated to the data. The reduced parameter set of this approach can resolve the overall mass balance but cannot by definition inform the internal space-time variation of physical processes. The Stanford watershed model is an early example of the lumped model that includes watershed processes [Crawford and Linsley, 1966]. There have been efforts to try to bridge these two approaches. Duffy [1996] describes a two-state model by integrating Richards' equation over a hillslope into saturated and unsaturated states, and later extended this approach to the problem of mountain-front recharge using hypsometry to partition the upland, transition, and flood plain zones into a intermediate-dimensional system [Duffy, 2004]. Reggiani *et al.* [1998, 1999] proposed a comprehensive semidistributed framework in which integrated conservation equations of mass, momentum, and energy are solved over a representative elementary watershed (REW). They discuss the issues involved in parameterizing the integral flux-storage relation at the REW scale, and refer to this as hydrologic closure.

[6] The decision of using a lumped, distributed, or semi-distributed approach to model watershed systems ultimately depends on the purpose of the model, and each has its advantages and disadvantages. For the distributed case, the governing equations are derived from local constitutive relationships. For instance, the Darcy equation is applicable at the plot or perhaps hillslope scale, but it is not clear what should be the effective relation of flux-to-state variable when integrated over larger scales where semidistributed or lumped models are used (e.g., the hydrologic closure problem discussed by Beven [2006]). At present there is considerable discussion in the literature about the relation of data needs and predictive models, including the issues of model type (lumped, semidistributed, distributed), uniqueness, and the appropriate scales of integration [Sivapalan *et al.*, 2002].

[7] In the present paper a new strategy for integrated hydrologic modeling is proposed that naturally handles physical processes of mixed partial differential equations (PDEs) and ordinary differential equations (ODEs) as a fully coupled system. The model formulates the local physical equations via the finite volume method, using geographic information systems (GIS) tools to decompose the model domain on an unstructured grid, as well as distributing a priori parameter estimates to each grid cell. In the limit of small-scale numerical grids, the finite volume method implements classical (e.g., continuum) constitutive relationships. For larger grid scales the method reflects the assumptions of the semidistributed approach described above, but with full coupling of all elements. The process of altering the physical model to accommodate effective parameterizations or new equations is a relatively simple process, since all equations reside in the same location in the code (i.e., the kernel). In this approach, the interactions are assembled on the right-hand side of the global ODE system, which is then solved with a state-of-the-art solver designed for stiff, nonlinear systems. The approach utilizes a triangular irregular grid that covers the domain with the fewest number of triangles [Palacios-Velez and Duevas-Renaud, 1986; Polis and McKeown, 1993] subject to constraints as defined by the particular problem.

## 2. Modeling Approach

### 2.1. Semidiscrete FVM Approach

[8] In this section we develop the finite volume approximation for an arbitrary physical process operating on an unstructured grid cell. A general form of the mass conservation equation for an arbitrary scalar state variable  $\chi$  can be written

$$\frac{\partial \chi}{\partial t} + \nabla \cdot \chi \mathbf{V} + \frac{\partial \chi}{\partial z} = \Omega_\chi, \quad (1)$$

where  $\chi$  represents mass fraction of storage (dimensionless). For convenience, the velocity vector in (1) is divided into horizontal ( $\mathbf{V} = \{u, v\}$ ) and vertical components  $\{w\}$ , and  $\Omega_\chi$  is a local source/sink term for the process represented by  $\chi$ . Volume integration of (1) proceeds in two steps: First, we integrate over the depth of the layer and then over the area. For a single layer of thickness  $z_a \leq z \leq z_b$  containing the scalar  $\chi$ , the integral over the depth takes the form

$$\begin{aligned} \frac{\partial}{\partial t} \int_{z_a}^{z_b} \chi dz - \chi_{z_b} \frac{\partial z_b}{\partial t} + \chi_{z_a} \frac{\partial z_a}{\partial t} + \nabla \cdot \int_{z_a}^{z_b} \chi \mathbf{V} dz - (V\chi)_{z_b} \nabla z_b \\ + (V\chi)_{z_a} \nabla z_a + (w\chi)_{z_a} - (w\chi)_{z_b} = \int_{z_a}^{z_b} \Omega_\chi dz \end{aligned} \quad (2)$$

We can evaluate the boundary terms, by rewriting equation (2) for a small layer about the boundary itself,  $z_b^- \leq z \leq z_b^+$ , where  $z_b^- = z_b - \varepsilon$  and  $z_b^+ = z_b + \varepsilon$ . Letting the layer thickness approach zero,  $z_b^+ - z_b^- \rightarrow 0$ , the integral terms are eliminated and the remaining terms must balance

as we approach the interface from both sides, leading to a definition of the net interface flux:

$$\chi_{b^+} \frac{\partial z_{b^+}}{\partial t} + (V\chi)_{b^+} \nabla z_{b^+} - (w\chi)_{b^+} = \chi_{b^-} \frac{\partial z_{b^-}}{\partial t} + (V\chi)_{b^-} \nabla z_{b^-} - (w\chi)_{b^-} = Q_b, \quad (3)$$

where  $Q_b$  is the net flux across  $z = z_b$ . A similar expression is found for  $Q_a$  at  $z = z_a$ . Equation (2) is now written in terms of vertically integrated storage in the layer:

$$\frac{\partial \bar{\chi}}{\partial t} + \nabla(V\bar{\chi}) = Q_b - Q_a + \omega, \quad (4)$$

where  $\bar{\chi}$  is the volumetric storage per unit area (L) in the layer defined by

$$\bar{\chi} = \int_{z_a}^{z_b} \chi dz, \quad (5)$$

and  $\omega$  is the vertically integrated source/sink term

$$\omega = \int_{z_a}^{z_b} \Omega_\chi dz. \quad (6)$$

To complete the volume integration, equation (4) is now written

$$\frac{\partial}{\partial t} \int_A \bar{\chi} dA + \int_\Gamma N(V\bar{\chi}) d\Gamma = \int_A (Q_b - Q_a + \omega) dA, \quad (7)$$

where the divergence theorem was applied to the second term,  $\Gamma$  is the perimeter of  $A$ , and  $N$  is the unit normal vector on  $\Gamma$ . Writing (7) in semidiscrete finite volume form [Leveque, 2002] yields

$$\frac{d\bar{\chi}}{dt} = \sum_{k=1}^2 Q_k - \sum_{i=1}^m Q_i, \quad (8)$$

where  $\bar{\chi}$  is now interpreted as the volumetric storage ( $L^3$ ) of  $\chi$  in the control volume (incompressible fluid),  $Q_i$  is net volumetric flux through the sides  $i = 1, 2, 3$  of the control volume, and  $Q_k$  is the net volumetric flux across the upper and lower boundaries  $k = 1, 2$ . Later it will be convenient to divide (8) by the projected horizontal surface area of the finite volume such that storage is an equivalent depth, and volumetric flux terms are normalized to a unit horizontal surface area.

[9] The vector form of equation (8) represents all processes  $\bar{\chi} = \{\chi_1, \chi_2, \dots, \chi_k\}$  within the control volume and forms a fully coupled local ODE system. The fluxes across the sides of the control volume are evaluated by appropriate constitutive (or closure) relationships for specific processes and applications. We note again that the finite volume method guarantees mass conservation for each control volume [Leveque, 2002], and that the semidiscrete representation reduces all equations to a standard form.

## 2.2. Multiscale, Multiprocess Formulation

[10] The next step in developing the multiprocess system is domain decomposition. The horizontal projection of the watershed area is decomposed into Delauney triangles. Each triangle is projected vertically to span the “active flow volume” forming a prismatic volume which is further subdivided into layers to account for the physical process equations and material layers. When governing equations are a mix of ODEs (e.g., vegetation interception) and PDEs (e.g., overland flow, groundwater flow), the PDEs are first reduced to ODEs by applying the semidiscrete finite volume method (FVM) approach described above, and then all ODEs are associated with a layer within the prism. The prism is where all physical equations (and thus all time-scales of the problem) reside, and we refer to this local system as the kernel. Assembling the local ODE system over the watershed domain, a global system is formed which is then solved with an efficient ODE solver. This solution method is also known as the “method of lines” [Madsen, 1975], here applied to a system of differential equations. For the multiple processes encountered in watershed research, the approach has several advantages. First, the model kernel representing all physical processes operating within the prismatic control volume can be easily modified for different applications or processes without altering the solver or even the domain decomposition. Since all physical equations are in a single subroutine, adding or omitting processes, material properties, or forcing makes modifications to the program quite simple. Second, the ODE is solved as a “fully coupled” system, with no time lagging or iterative linking of processes. Third, alternative constitutive or closure relationships are also easily implemented and tested in this strategy. The constitutive relationship might come from conceptual models, numerical experiments [Duffy, 1996], or theoretical derivation [Reggiani et al., 1999; Reggiani and Rientjes, 2005]. It is noted that constitutive relationships are sensitive to the scale of volume integration [Beven, 2006], a feature that is natural to the semidiscrete approach used here.

[11] In this research we are developing an open-source community code for the simulation of watersheds and river basins, and we refer to this code as PIHM: Penn State Integrated Hydrologic Model. In this first generation of PIHM, we consider the following processes and dimensions: one-dimensional (1-D) channel routing, 2-D overland flow, and 2-D subsurface flow are governed by PDEs, while canopy interception, evapotranspiration, and snowmelt are described by ODEs. Each process is assigned to a layer within the kernel with overland flow and channel flow assigned to the surface layer, and the channel centered on any edge of the element. Prior to domain decomposition, the river network, hydraulic structures, or other devices, such as dams, gages, weirs, etc., are identified as special points used to constrain the decomposition. Although it imposes some computational burden to the grid generation, this idea simplifies the geometry of the decomposed region, which in turn facilitates assembling the global ODE system. For example, this step will guarantee that no channel intersects the control volume interior, or the channel segments are always centered on the boundary between two watershed elements. It also locates gages (stage, well level, climate station) at vertices of elements where desired, simplifying

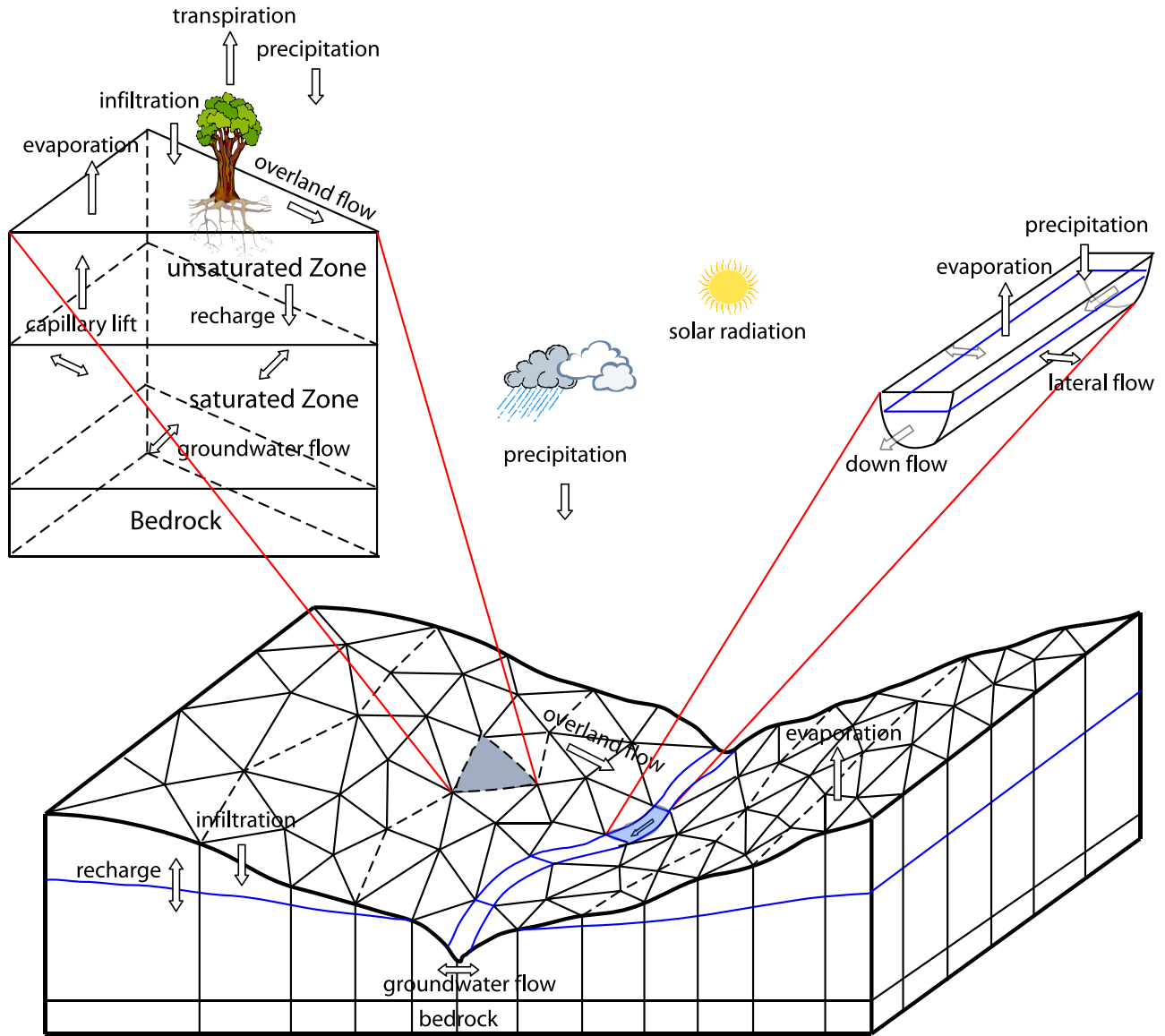


**Figure 1.** Schematic view of domain decomposition for hillslopes and stream reach. The finite volume elements are prisms projected from the triangular irregular grid also referred to as a TIN (triangular irregular network). The TIN is generated with channels as constraints, which will guarantee that the channel is along the element boundary. In the upper part of the figure, the basic element is shown to the left with multiple hydrological processes. A channel segment for a triangle bounded by a stream is shown to the right.

postprocessing. Figure 1 illustrates the decomposition and kernel for the system to be studied here.

### 3. Building the Local ODE System

[12] The choice of equations in any situation is a practical balance of the most important physical processes assumed to operate on a watershed (Shale Hills, in our case), the assumptions made about these processes in a particular representation, and the scale of computation. We note that there are no intrinsic limitations to more complex (or simpler) equations/processes. Those presented here are sufficient to characterize the physics of the particular physical setting we have chosen to demonstrate.

### 3.1. Processes Governed by PDEs

#### 3.1.1. Surface Overland Flow

[13] The governing equations for surface flow are the 2-D St. Venant equations. *Sleigh et al.* [1998] have developed a numerical algorithm solving the full St. Venant equations using the finite volume method for predicting flow in rivers and estuaries, where the normal flux vector is calculated using Riemann approach [Leveque, 2002], and we follow their approach here. Letting  $\bar{\chi} \rightarrow h_o(x, y, t)$ , the vertically integrated form of the continuity equation (4) is given by

$$\frac{\partial h_o}{\partial t} + \frac{\partial(uh_o)}{\partial x} + \frac{\partial(vh_o)}{\partial y} = \sum_{k=1}^2 q_k, \quad (9)$$



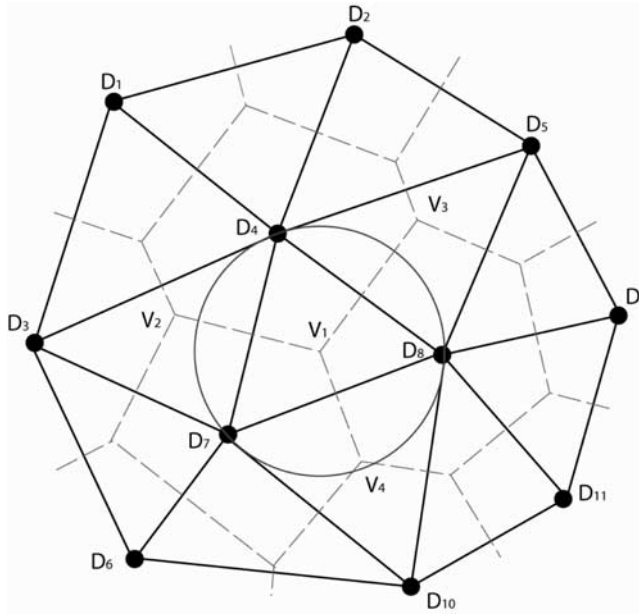


**Figure 2.** Delaunay triangulation and Voronoi diagram. The solid lines form Delaunay triangles, and the dashed lines form Voronoi polygons. The circumcenter  $V_i$  is the vertex of the perpendicular bisectors of the triangle, and is used to represent the triangle for the volume average of the state variable.

where  $h_o(x, y, t)$  is the local water depth. Here  $u$  and  $v$  are velocities in the plane  $x, y$ ;  $q_k$  are the surface flux terms normalized by surface area. Note that there are three unknowns,  $h_o$ ,  $u$ , and  $v$ , for each element. To reduce the complexity of solving the full St. Venant equations, we neglect inertia terms in the momentum equation, and Manning's formula is used to close equation (9), which yields the diffusion wave approximation [Gottardi and Venutelli, 1993]

$$\frac{\partial h_o}{\partial t} = \frac{\partial}{\partial x} \left( h_o k_s \frac{\partial H}{\partial x} \right) + \frac{\partial}{\partial x} \left( h_o k_s \frac{\partial H}{\partial x} \right) + \sum_k q_k \quad (10)$$

with

$$k_s = \frac{h_o^{\frac{2}{3}}}{n_s} \frac{1}{|\partial H / \partial s|^{\frac{1}{2}}}, \quad (11)$$

where  $H(x, y, t)$  is the water surface elevation above an horizontal datum,  $n$  is Manning roughness coefficients,  $s = s(x, y)$  is the vector direction of maximum slope, and  $q_k$  are the layer top and bottom input/output.

[14] Since the basic element in our implementation is a vertically projected prism (Figure 1), the evaluation for  $k_s$  is slightly complicated. Let  $(x_i, y_i, H_i)$  be the local coordinates of the free water surface at vertex  $V_i$ . Assume the free surface plane is determined by vertex  $V_2, V_3, V_4$  and that the

triangular element of  $D_4D_7D_8$  is identical. The plane is then defined by (see Figure 2)

$$\begin{vmatrix} x & y & H & 1 \\ x_2 & y_2 & H_2 & 1 \\ x_3 & y_3 & H_3 & 1 \\ x_4 & y_4 & H_4 & 1 \end{vmatrix} = 0. \quad (12)$$

Note that

$$\frac{\partial H}{\partial s} = \frac{s}{\|s\|} \cdot \nabla H,$$

and thus the hydraulic head gradient along the maximum slope direction of element  $D_4D_7D_8$  is given by

$$\frac{\partial H}{\partial s} = \sqrt{\left( \frac{(y_3 - y_2)(H_4 - H_2)}{(x_2 - x_3)(H_4 - H_2)} \right)^2 + \left( \frac{(x_4 - x_2)(H_3 - H_2)}{(x_3 - x_2)(H_4 - H_2)} \right)^2}. \quad (13)$$

For elements that border a channel, special handling is required, and we discuss this in section 3.1.3. For the diffusion wave approximation, the surface flux per unit width of flow is given by

$$Q_s = h_o k_s \frac{\partial H}{\partial s}, \quad s = s(x, y) \quad (14)$$

using (11) and (13). Applying the semidiscrete approach discussed above to equation (10) and normalizing by the surface area of the element yields the semidiscrete approximation for overland flow

$$\left( \frac{dh_o}{dt} = p - q^+ - e + \sum_{j=1}^3 q_j^s \right)_i, \quad (15)$$

where  $q_j^s$  is the normalized lateral flow rate from element  $i$  to its neighbor  $j$ . The terms  $p$ ,  $q^+$ , and  $e$  are throughfall precipitation, infiltration, and evaporation, respectively.

### 3.1.2. Subsurface Flow

[15] For subsurface flow we start again from (1) and let our scalar be the moisture content (volume water/void volume),  $\chi \rightarrow \theta$ , which we write (1) as

$$\frac{\partial \theta}{\partial t} + \nabla \theta V + \frac{\partial (w\theta)}{\partial z} = +S_\theta, \quad (16)$$

where once again the divergence terms are separated into vertical ( $w$ ) and horizontal  $V = (u, v)$  components. Flow within the subsurface layer is complicated by the existence of a free surface boundary or water table within the layer. The layer is partitioned into two parts, where the soil above the water table ( $z^+$ ) is governed by gravitational and surface

tension forces, while gravity alone governs below the water table ( $z^-$ ). Using (2) and (3) and integrating over the depth of the layer yields

$$\begin{aligned}\theta_s \frac{\partial h_u}{\partial t} + \nabla(\theta V h_u) &= q^+ - q^o \\ \theta_s \frac{\partial h_g}{\partial t} + \nabla(\theta V h_g) &= q^o - q^-.\end{aligned}\quad (17)$$

The divergence terms in (17) represent horizontal flow in the unsaturated (plus sign) and saturated (minus sign) parts of the layer,  $\theta_s$  is the moisture content at saturation,  $h_u$  is the equivalent depth of moisture storage above the water table, and  $h_g$  is the depth of saturation below the water table defined by

$$h_u = \int_{z_o^+}^{z_b} \frac{\theta}{\theta_s} dz, \quad h_g = \int_{z_a}^{z_o^-} \frac{\theta_s}{\theta_s} dz, \quad (18)$$

where the layer is now defined with two complementary zones above ( $z_a \leq z \leq z_o^+$ ) and below the water table ( $z_a \leq z \leq z_o^-$ ). The flux terms or source terms to the soil moisture zone ( $q^+$  and  $q^o$ ) are defined respectively as infiltration/exfiltration through the soil surface, and recharge to and from the water table. The flux  $q^-$  admits an exchange with a deeper groundwater layer. The divergence terms for lateral flow are evaluated by integrating (17) over the projected surface area of the control volume (Figure 1). Applying the Reynolds transport theorem [Slattery, 1978] and the divergence theorem yields equations for flow above and below the water table, respectively:

$$\begin{aligned}\frac{1}{A} \int_A \nabla(\theta V h_u) dA &= \frac{1}{A} \int_B (\theta V h_u) n dB \simeq \sum_{j=1}^3 q_j^u \\ \frac{1}{A} \int_A \nabla(\theta V h_g) dA &= \frac{1}{A} \int_B (\theta V h_g) n dB \simeq \sum_{j=1}^3 q_j^g.\end{aligned}\quad (19)$$

See Duffy [1996] for details. Finally, the balance equations are formed for a fully coupled unsaturated-saturated flow within the layer,

$$\begin{aligned}\theta_s \frac{dh_u}{dt} &= q^+ - q^o + \sum_{j=1}^3 q_j^u \\ \theta_s \frac{dh_g}{dt} &= q^o - q^- + \sum_{j=1}^3 q_j^g,\end{aligned}\quad (20)$$

where the unsaturated and saturated depth of storage ( $h_u, h_g$ ) are now interpreted as volume averages per unit projected horizontal surface area. The divergence terms in (20) define the net lateral soil moisture flux and net lateral groundwater exchange with adjacent elements. From this point we will assume that the flow is vertical in the unsaturated zone, but that lateral saturated groundwater flow is

$$\sum_{j=1}^3 q_j^g \neq 0.$$

We note that this term also represents stream-aquifer interaction for elements adjacent to a channel. The net flux

to/from the water table  $q^0(h_u, h_g)$  represents the integral properties of unsaturated flow and recharge to/from the water table, as well as the effect of water table fluctuations. Again, in the governing ODEs all fluxes are normalized by projected horizontal surface area of the element with units [L/T].

[16] For applications where the Darcy relationship is appropriate, lateral groundwater fluxes are evaluated using its volume-average form [Duffy, 2004] given by

$$q_{ij}^g = B_{ij} K_{eff} \frac{(H_g)_i - (H_g)_j}{D_{ij}} \frac{(h_g)_i + (h_g)_j}{2}, \quad (21)$$

where  $B_{ij}$  is length of common boundary and  $D_{ij}$  is distance between the circumcenters of elements  $i$  and  $j$ .  $(H_g = h_g + z)_i$  is hydraulic head where  $z_i$  is elevation of datum of element  $i$ . The effective hydraulic conductivity  $K_{eff}$  is the harmonic mean of the hydraulic conductivity in element  $i$  and  $j$ . The storage-discharge relation in equation (21) is nonlinear due to vertical integration. Brandes [1998] also shows, by way of numerical experiments, that the integral storage-discharge or “effective” constitutive relationship is a nonlinear function of hydraulic head at the hillslope scale. Flexible constitutive relationships from conceptual models, numerical experiments, and theoretical derivations can be introduced where deemed appropriate.

[17] The approach used here assumes that each subsurface layer in the model can have both saturated and unsaturated storage components. The interaction or coupling term between the unsaturated and saturated storage is defined by  $q^0$ , the recharge or water table flux in equation (20). Duffy [2004] developed a simplified analytic expression for the flux of recharge to/from a water table based on integration over the unsaturated portion of the layer using a simple exponential-type soil characteristic [Gardner, 1958], which has the form

$$q^0(h_u, h_g) = K_s \frac{1 - e^{-\alpha(z_s - h_g)} - \alpha h_u}{\alpha(z_s - h_g) - (1 - e^{-\alpha(z_s - h_g)})}, \quad (22)$$

where  $K_s$  is saturated hydraulic conductivity. The  $\alpha$  is a soil texture parameter for the exponential soil model;  $z_s$  is total layer thickness. The integrated internal flux at the water table  $q^o$  is a nonlinear function of the water table position and the depth of soil moisture storage above the water table. Equation (22) is shown for a clay loam soil in Figure 3 after Duffy [2004]. It is noted that although *van Genuchten* [1980] or *Brooks and Corey* [1964] formulations are more generally used in discretized form, the recharge function (22) has the advantage of simplicity and computation speed.

[18] The general point is that the kernel is easily edited for the desired constitutive or closure relation, with proper care taken for new parameters required by the formulation. A special situation occurs under shallow water table conditions, where unsaturated storage is approximated by a simple function of the saturated storage and the system (20) can be reduced. This idea is developed for a particular case in section 6.

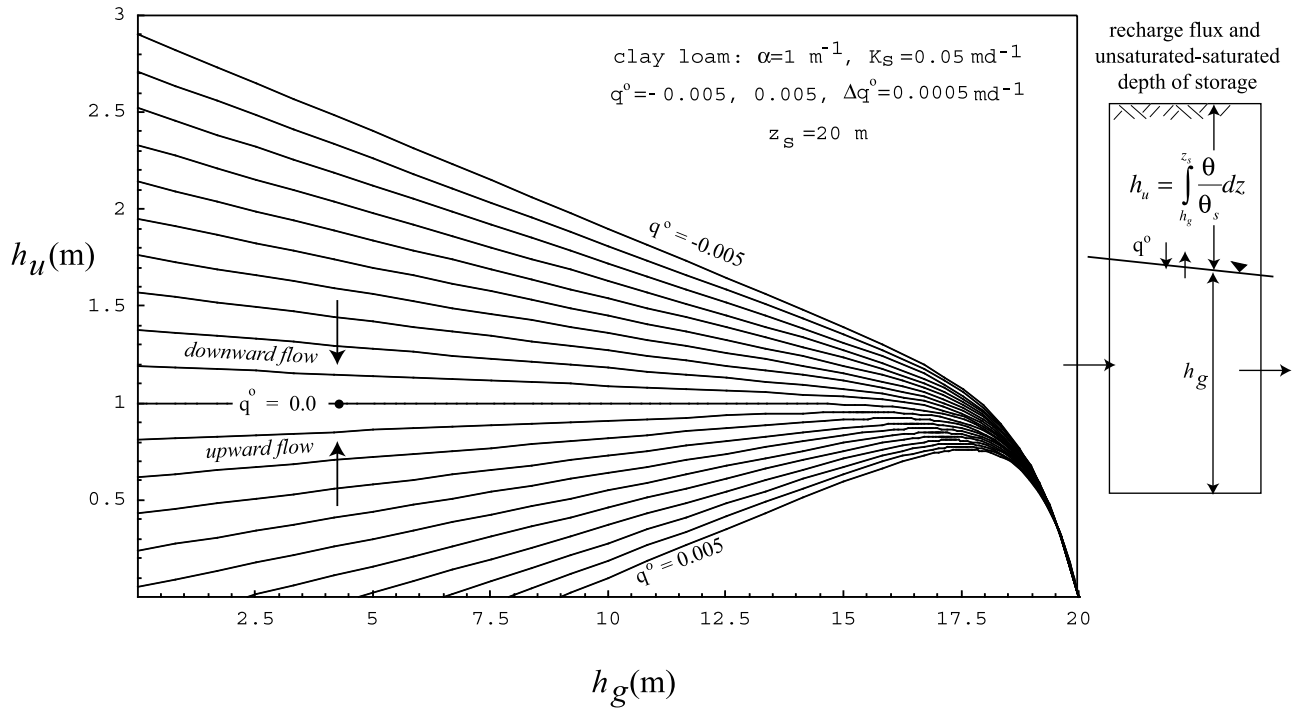


**Figure 3.** Illustration of the theoretical recharge  $q^o$  [ $LT^{-1}$ ] or flux of water to/from a water table within a partially saturated layer based on equation (22). The figure shows the relationship of unsaturated and saturated storage with recharge, and is based on a solution to Richard's equation for an exponential-type soil characteristic [Duffy, 2004]. For this example we neglect lateral flow in the unsaturated zone.

### 3.1.3. Channel Routing

[19] For channel routing, applying the semidiscrete approach to the 1-D Saint Venant equations with the same assumptions as overland flow yields

$$\left( \frac{dh_c}{dt} = p - e + \sum_{i=1}^2 (q_i^s + q_i^g) + q_{in}^c - q_{out}^c \right)_i, \quad (23)$$

where  $h_c$  is depth of water in the channel,  $p$  and  $e$  are precipitation and evaporation for the channel segment, and  $q_i^s$  and  $q_i^g$  are the lateral interaction terms for the aquifer and surface flow from each side of the channel. The upstream and downstream channel segments are  $q_{in}^c$  and  $q_{out}^c$ , respectively. The volumetric fluxes are normalized by the horizontally projected surface area of the channel segment, where the channel is a 1-D prismatic volume with a trapezoidal or other cross section. As in the case of overland flow, the diffusion wave approximation is applied to the upstream and downstream channel flux terms.

[20] The interaction of surface overland flow and channel routing,  $q_i^g$  in equation (15) and (23), is controlled by a weir-type equation following Panday and Huyakorn [2004]. For the case of channel flooding (i.e., the channel depth exceeds critical depth), the condition becomes a submerged weir where the discharge is a function of flow depth in surface overland flow and the channel segment. The interaction between the saturated groundwater flow and channel routing  $q_i^g$  in equation (20) and (23) is governed by the discrete form of the Darcy equation as in (21) where the adjacent head is the depth of the channel.

[21] The interaction between the surface flow and sub-surface flow is controlled by two runoff generation mechanisms. When there is ponding on the surface, the infiltration rate in equation (15) and (20) is a function of the soil moisture, with the upper bound the max infiltration capacity (e.g., a bounded linear relation). If the layer is fully saturated, then the runoff is generated by subsurface saturation (Dunne runoff generation mechanism), and the precipitation is rejected within that time step.

## 3.2. Processes Governed by ODEs

### 3.2.1. Interception Process

[22] In the presence of vegetation and canopy cover, a fraction of precipitation is intercepted and temporally stored until it returns to the atmosphere as evaporation, or passes through the canopy as throughfall or stemflow. In this case the conservation equations are directly written as balance equations in ODE form. Assuming that spatial interactions of canopy storages among elements are insignificant, the governing equation has the form

$$\left( \frac{dh_v}{dt} = p_v - e_v - p \right)_i, \quad (24)$$

where  $h_v$  is vegetation interception storage. Here  $p_v$  is total water equivalent precipitation,  $e_v$  represents evaporation from surface vegetation, and  $p$  is throughfall and stemflow or effective precipitation to surface storage in equation (15). The upper bound of  $h_v$  is a function of vegetation type, canopy density, and even the precipitation intensity

[Dingman, 1994]. When the canopy reaches the upper threshold, all precipitation becomes throughfall.

### 3.2.2. Snowmelt Process

[23] The accumulation and melting process of snow is a cold-season counterpart to interception. Although a more comprehensive physics of snow could be applied, here we use a simple index approach to snow accumulation and melt [Dingman, 1994]. Assuming that vegetation is dormant during the snow season, and while air temperature is below snow-melting temperature  $T_m$ , the snowpack will accumulate during precipitation, and if air temperature exceeds the melting temperature the snowpack melts. The dynamic snowmelt conservation equation is given by

$$\left(\frac{dh_s}{dt} = p_s - e_s - \Delta w\right)_i, \quad (25)$$

where  $\Delta w$  is snow melting rate, which is also an input to overland flow. It can be calculated by the air temperature with

$$\Delta w = \begin{cases} M(T_a - T_m), & T_a > T_m \\ 0, & T_a \leq T_m, \end{cases} \quad (26)$$

where  $M$  is melt factor, which can be estimated from empirical formulas [Dingman, 1994], and  $e_s$  is evaporation directly from snow.

### 3.2.3. Evaporation and Evapotranspiration

[24] Evaporation from vegetation interception, overland flow, and snow and river surfaces is estimated using the Pennman equation [Bras, 1990], which represents a combined mass-transfer and energy method:

$$\left(e = \frac{\Delta(R_n - G) + \rho_a C_p (\varepsilon_s - \varepsilon_a)}{\Delta + \gamma}\right)_i. \quad (27)$$

Potential evapotranspiration from soil and plant is estimated using Pennman-Monteith equation

$$\left(et_0 = \frac{\Delta(R_n - G) + \rho_a C_p \frac{(\varepsilon_s - \varepsilon_a)}{r_a}}{\Delta + \gamma \left(1 + \frac{r_s}{r_a}\right)}\right)_i. \quad (28)$$

Here  $et_0$  refers to potential evapotranspiration,  $R_n$  is net radiation at the vegetation surface,  $G$  is soil heat flux density,  $\varepsilon_s - \varepsilon_a$  represents the air vapor pressure deficit, and  $\rho_a$  is the air density,  $C_p$  is specific heat of the air.  $\Delta$  is slope of the saturation vapor pressure-temperature relationship,  $\gamma$  is the psychrometric constant, and  $r_s$ ,  $r_a$  are the surface and aerodynamic resistances. Actual evapotranspiration is a function of potential  $et_0$  and current plant, climatic, and hydrologic conditions, such as soil moisture. In the implementation, coefficients are introduced to calculate actual ET from potential following Kristensen and Jensen [1975]. Allen *et al.* [1998] provides guidelines used here for computing those coefficients for different vegetation.

[25] Combining equations (15), (20), (23), (24), and (25) leads to a local system of ODEs representing multiple hydrological processes within the prism or kernel element  $i$ . Spatial interactions are evaluated with appropriate consti-

tutive or closure relationships for (14), (21), (22), (26), and (27).

[26] A central feature of the integrated model PIHM is that all processes are fully coupled, first through the local kernel, and then in the global ODE system. Here we have outlined the interactions between major hydrologic processes, e.g., surface overland flow, unsaturated subsurface flow, saturated subsurface flow, and channel routing. More details can be found in the dissertation by Qu [2005].

## 4. Assemble Global ODE System

[27] The global ODE system is formed by assembling the local system of equations (e.g., the kernel) and assigning cell-to-cell connections over the watershed domain. Generation of the unstructured grid involves domain decomposition into prismatic volumes. The unstructured grid generation attempts to achieve the fewest number of cells to cover the region, while satisfying specific constraints (e.g., rivers form along the edge of a cell, cells should be as close to equilateral as possible for a quality grid, etc.).

[28] We apply Delaunay triangulation [Delaunay, 1934; Voronoi, 1907; Du *et al.*, 1999] to form an orthogonal triangular unstructured grid [see Palacios-Velez and Duevas-Renaud, 1986; Polis and McKeown, 1993; Vivoni *et al.*, 2004]. The grid is optimal in the sense that each triangle is as close to equilateral as possible, for a given set of constraints. The constraints can include watershed boundaries, the stream network, geologic boundaries, elevation contours, or hydraulic structures. After completion of the domain decomposition, the triangular irregular network (TIN) is projected vertically downward to form prismatic volume elements, as shown in Figures 1 and 2. Using the circumcenter as the node defining each triangle instead of the centroid of the cell assures that the flux across any edge with its neighbor is normal to the common boundary. For instance,  $V_1V_2$  is normal to  $D_4D_7$  in Figure 2. This simplifies evaluation of the flux across each boundary. However, it has the restriction that the circumcenter must remain within the triangle under all circumstances. Shewchuk [1997] has developed an algorithm that computes the Delaunay triangulation satisfying the above requirement from a set of points and constraints, in principle, and we adopt this algorithm here.

[29] Grid generation for the watershed domain starts from a set of defined control points. In general, the goal is to represent the terrain with a minimum of triangles and special constraints, such as hydrographic points (e.g., gaged sites, dams etc.), and other specified critical terrain points (e.g., local topographic maximum/minimum, convexity/concavity, or saddle points). These special points are selected using terrain analysis tools. Once selected, they are honored for any subsequent grid generation. In addition to special points, we can also use line segments from catchment boundaries such as the stream network, elevation contours, vegetation polygons, etc., as constraints in the grid generation. This preserves certain natural boundaries in the domain decomposition for a particular problem. Usually the goal is to generate a mesh having as small a number of elements as possible while still satisfying all requirements of the Delaunay triangle (minimum angle, maximum area, and constraints, etc.), and meeting the goals of the hydro-



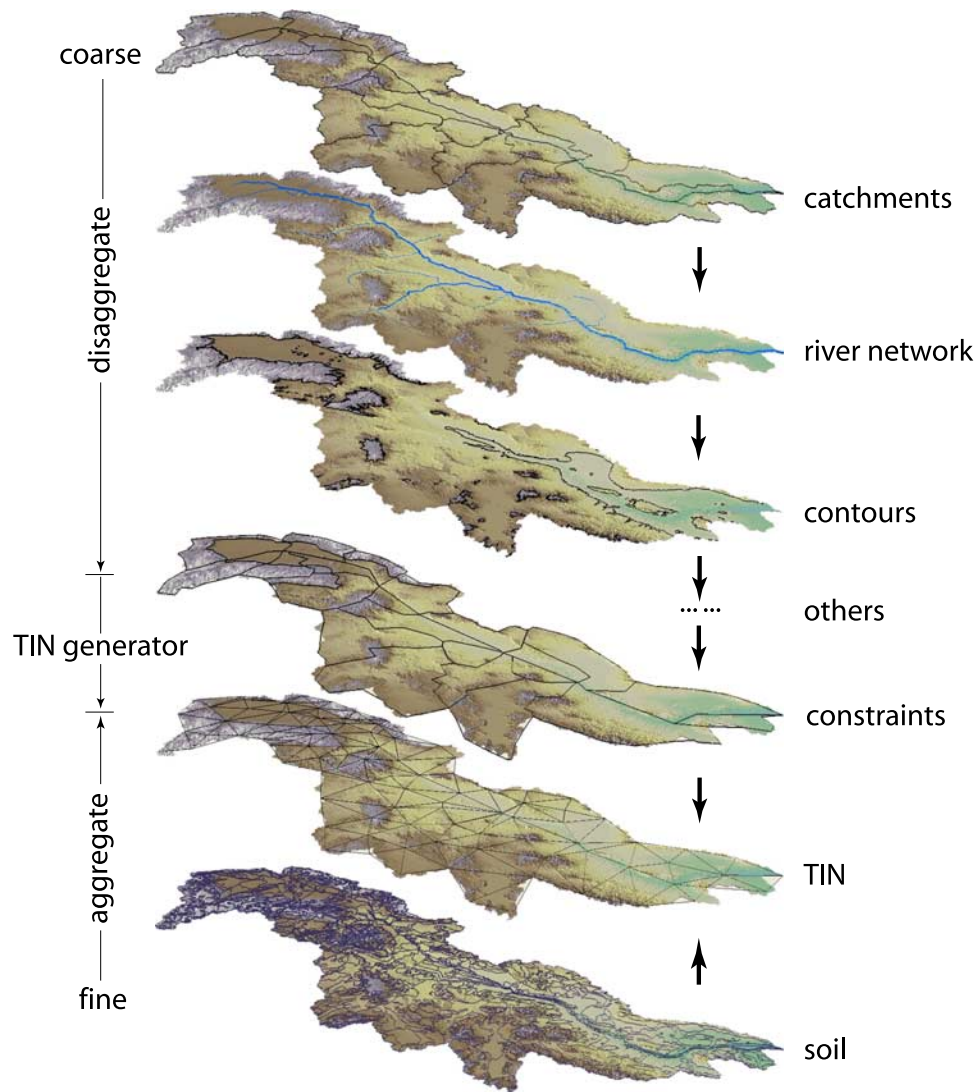


**Figure 4.** Schematic view of the steps in domain decomposition. During the disaggregating process, catchments boundary, river network, and critical terrain points, etc., are introduced as constraints for generation of the TIN. GIS tools along with soil survey and/or geologic maps are utilized to assign a priori hydraulic properties for each model element.

logic simulation (minimum support for the river network, minimum channel length increment, etc.).

[30] Figure 4 illustrates the sequence of procedures used to generate the grid and estimate parameters for each element in a river basin. The decomposition process involves delineation of the catchments boundary and river network at the desired resolution (support), given the constraint framework. The constraints, often delineated from digital elevation data or other related coverages [Tarboton *et al.*, 1991; Palacios-Velez *et al.*, 1998; Maidment, 2002], clearly play a very important role in domain decomposition.

[31] Careful matching of the special point and line constraints including the channel network, with the choice of minimum area support (resolution), will assure that the domain boundaries are consistent before domain decomposition. Once the grid is generated, a priori parameter fields

from the GIS (soil and geologic hydraulic properties, vegetation parameters, etc.) are projected onto the grid.

## 5. Solving the Global ODE System

[32] Combining the local ODE system across the solution domain yields a global ODE system in form

$$My' = f(t, y; x), \quad (29)$$

where  $M$  is the identity matrix,  $y$  is an  $n$  by 1 vector of state variables, and  $x$  is the forcing. The unknown states are fully coupled on the right-hand side of equation (29).

[33] An explicit solver is always preferred if an acceptable solution can be achieved, since within each time step, an explicit solver requires fewer evaluations of the right-hand side. However, the multiple timescales arising from

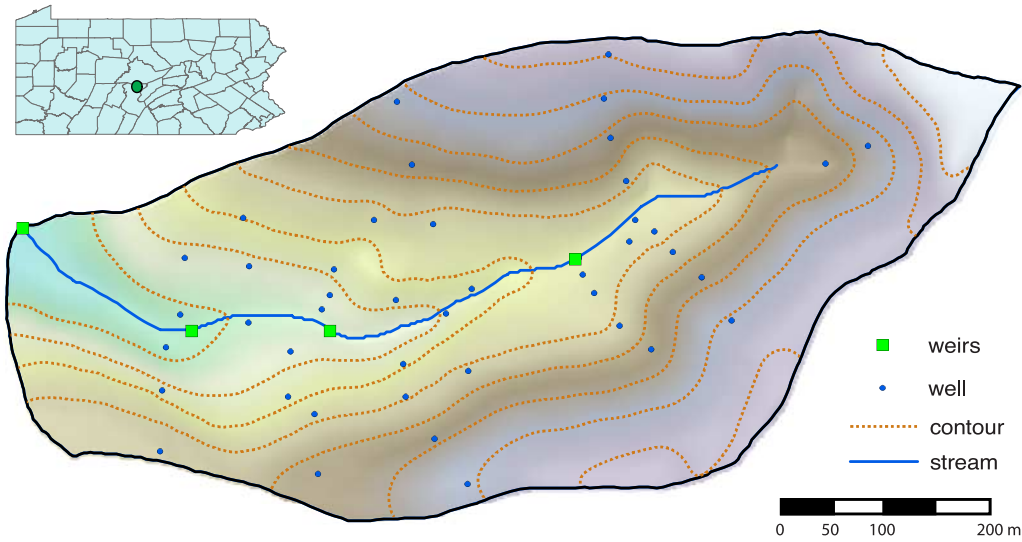


**Figure 5.** The Shale Hills watershed and measurement locations. It consists of 44 wells, 44 neutron probes, and four weirs distributed over the 19-acre watershed.

watershed processes typically make (29) a highly stiff system [Ascher and Petzold, 1998]. For stiff problems, the overall computational cost of an explicit solution may actually be higher than an implicit solver due to stability concerns. The implicit sequential solver used here is the SUNDIALS package (suite of nonlinear and differential/algebraic equation solvers), developed at the Lawrence Livermore National Laboratory. The code has been widely applied, with extensive testing, and with excellent support.

[34] For the initial condition  $y(t_0) = y_0$ , a multistep formula is written

$$\sum_{i=0}^{K_1} \alpha_{n,i} y_{n-i} + h_n \sum_{i=0}^{K_2} \beta_{n,i} y'_{n-i} = 0, \quad (30)$$

where  $\alpha$  and  $\beta$  are coefficients. For stiff ODEs, CVODE [Cohen and Hindmarsh, 1994] in the SUNDIAL package applies the backward differentiation formula (BDF) with an adaptive time step and method order varying between 1 and 5. Applying (30) to (29) yields a nonlinear system of the form

$$G(y_n) \equiv y_n - h_n \beta_{n,0} f(t_n, y_n) - a_n = 0 \quad (31)$$

with

$$a_n \equiv \sum_{i>0} (\alpha_{n,i} y_{n-i} + h_n \beta_{n,i} y'_{n-i}). \quad (32)$$

Numerically solving equation (31), with some variant of Newton iteration, is equivalent to iteratively solving a linear system of the form

$$M(y_{n(m+1)} - y_{n(m)}) = -G(y_{n(m)}), \quad (33)$$

where  $M$  is  $I - h\beta_{n,0}J$  with  $J = \partial f / \partial y$ .

[35] The GMRES (generalized minimal residual) iterative linear solver in SUNDIAL makes the computational cost of solving the global ODE system very competitive when compared with other open-source solvers.

## 6. The Shale Hills Field Experiment

[36] The Shale Hills hydrologic experiment was conducted on a 19.8-acre watershed in the Valley and Ridge physiographic province of central Pennsylvania in 1974 by the Forest Hydrology group at the Pennsylvania State University [Lynch and Corbett, 1985; Lynch, 1976]. The objectives of the experiment were to determine the physical mechanisms of runoff and streamflow generation at the upland forested watershed, and to evaluate the effects of antecedent soil moisture on the runoff peak and timing. The fully coupled numerical model PIHM described earlier is now applied to the Shale Hills site. The goal is to generally explore the questions of the original field experiment using an integrated model. Specifically these include the following: (1) What is the impact of groundwater flow and soil moisture on stream runoff and peakflow generation? (2) What



**Figure 6.** Spray irrigation devices are regulated to control the rate of irrigation under the tree canopy during the Shale Hills experiment.

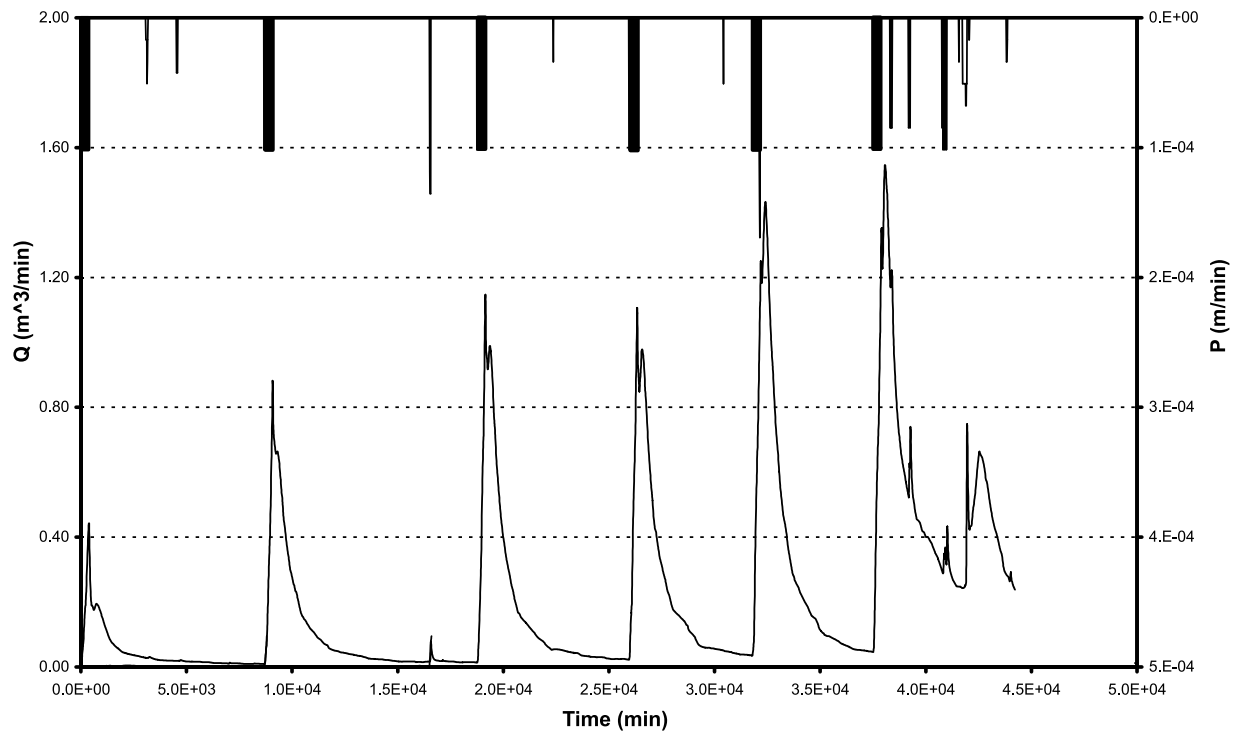


**Figure 7.** The six artificial rainfall events of equal magnitude and duration and the corresponding runoff at the outlet weir for the Shale Hills experiment.

is the role of complex topography in producing runoff at Shale Hills? (3) Can fully coupled models improve the ability to simulate catchments that have ephemeral and/or intermittent channels?

### 6.1. Experimental Design and Data

[37] The design consisted of a comprehensive network of 40 piezometers, 40 neutron access tubes for soil moisture, and four weirs. The distribution of sampling sites is shown in Figure 5. The upper part of the channel is ephemeral or intermittent, flowing during large storms or during the seasonal snowmelt period. The watershed was implemented with a spray irrigation network, shown in Figure 6, to precisely control the amount of artificial rainfall over the entire watershed. The irrigation was applied below the tree canopy and above forest litter, eliminating canopy interception storage during irrigation events. The watershed has a mixed deciduous and coniferous canopy, with a relatively thick forest litter. The soil profile at Shale Hills is typically a silt loam, ranging from 0.6-m thickness at the ridge top, to 2.5 m deep near the channel. Three soil types are identified as Ashby, a shaley-silt loam in the upland portion of the watershed; the Blairton silt loam on the intermediate elevation slopes; and the Ernest silt loam in the lower region along the channel. Underlying the soil is the Rose Hill Shale, which is thought to have a relatively low permeability [Lynch, 1976] and acts as an effective barrier to deeper flow. The bedrock topography was estimated by the limit of hand augering through the soil profile to bedrock.

[38] From July to September 1974, a series of six equal artificial rainfall events (0.64 cm/h for 6 hours) were applied to the entire watershed [Lynch, 1976]. The events were timed such that the antecedent moisture gradually increased from very dry in the first storm, to near saturation after the

last event. Along with the artificial rainfall, a few natural rainfall events also occurred. We note that the experiment was conducted in late summer through the fall season when evapotranspiration is small, and when the snow and frost could be neglected. Many irrigation treatments were conducted during this experiment. The data chosen here specifically reflect an experiment to test the effect of antecedent moisture on peak runoff by sequential storm events of the same rate and duration.

### 6.2. Water Budget

[39] Figure 7 illustrates the forcing and runoff data measured at 15-min intervals from late July to early September. Note the six artificial rainfall (irrigation) events, as well as natural rainfall. Natural rainfall would of course be applied to the top of the canopy. Nonetheless, during the late season we assume interception storage to be small and can be neglected.

[40] From the field data, the runoff/precipitation ratio is calculated for each rainfall event and the results are given in Table 1. The mass balance indicated that 4% of rainfall

**Table 1.** Observed Cumulative Input/Output and Runoff Ratio for the 1974 Rainfall-Runoff Experiment at Shale Hills

Event	Duration	Irrigation, m	Input, m <sup>3</sup>	Output, m <sup>3</sup>	Runoff/Precipitation Ratio, %
1	1–7 Aug	0.04318	3355.236	407.4109	12.1
2	7–14 Aug	0.045974	3572.339	998.8983	279
3	14–19 Aug	0.038608	2999.975	1287.057	42.9
4	19–23 Aug	0.038862	3019.712	1340.731	44.4
5	23–27 Aug	0.04064	3157.869	1839.37	58.2
6	27–31 Aug	0.071628	5565.744	3530.845	63.4
Total	1–31 Aug	0.2789	21670.88	9404.31	43.4

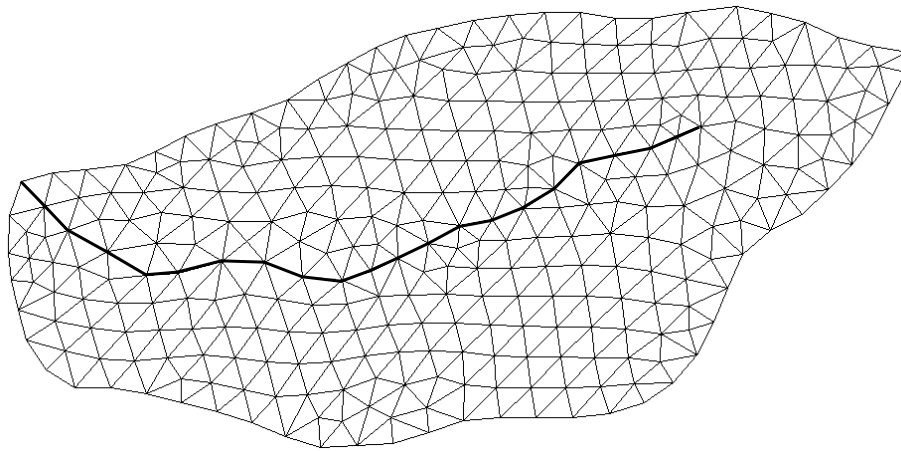


**Figure 8.** The unstructured grid used to simulate the watershed response for the Shale Hills watershed.

could not be accounted for in the runoff. This “error” may be due to insufficient density of measurements, missing processes, or parameters (i.e., interception or deep loss to bedrock).

### 6.3. Antecedent Soil Moisture Effect

[41] By conducting the experiment with equal rainfall events (0.64 cm/h for 6 hours), it is possible to test the effect of initial condition or antecedent moisture on runoff yield. We note that there was no significant infiltration-excess overland flow observed during the experiment. Apparently the infiltration capacity is large enough to accommodate the rainfall rate without producing overland flow. However, the deep forest litter makes this observation problematic. Figure 7 and Table 1 both indicate that as the antecedent moisture increases from a very dry to a very wet pre-event condition, the peak flow and total runoff increases as well, with only 12% of rainfall becoming runoff for the first storm (very dry), and 63% runoff ratio for very wet conditions. The relaxation for the sixth event in Figure 7 and the runoff ratio in Table 1 clearly suggest the significance of soil moisture and groundwater storage on the changing moisture threshold for rainfall-runoff generation. This is examined in more detail with the integrated model implementation next.

### 6.4. Model Domain and a Priori Data

[42] The surface terrain at Shale Hills is represented by a 1-m resolution digital elevation model (DEM) digitized from a detailed topographic survey of the watershed. There were 44 monitoring wells/neutron probes covering the domain as shown in Figure 5. The bedrock elevation was measured at piezometer locations and then interpolated to the whole domain. The domain is decomposed into 566 triangle elements with 315 nodes (Figure 8). The channel is delineated from the DEM with 21 segments, including both ephemeral and permanent reaches. Surface infiltration capacity is set to be the same as saturated hydraulic conductivity. Surface roughness varies with flow depth and surface obstacles [Hauser, 2003]. In this case, an effective surface roughness was estimated (trial and error) to be  $0.83 \text{ min}^{-1/3}$ . The precipitation/irrigation forcing was shown in Figure 7. Only daily temperature was available near the site, so daily data were used to get a rough estimate of evapotranspiration. The channel was assumed to be

rectangular, 1.5 m wide and 0.5 m deep. The hydraulic roughness for the channel is set to  $0.5 \text{ min}^{-1/3}$ . The watershed boundary condition was assumed no flow for surface and groundwater, and at the outlet of the catchment the channel was assumed to be at critical depth. All initial conditions were estimated by interpolation of neutron probe and observation well data to the value just prior to the first irrigation.

[43] The vertical profiles of soil moisture and saturated thickness with locations shown in Figure 5 were measured just before and after each irrigation and again at intervals between irrigations in the experiment. The spatial average depth of soil moisture storage ( $\bar{h}_u$ ) across the entire site was calculated and plotted against the spatial average saturated groundwater storage ( $\bar{h}_s$ ) and is shown in Figure 9. It reveals a strong correlation between saturated and unsaturated storage. Soil hydraulic properties were estimated from this information, and the procedure is described in the next section.

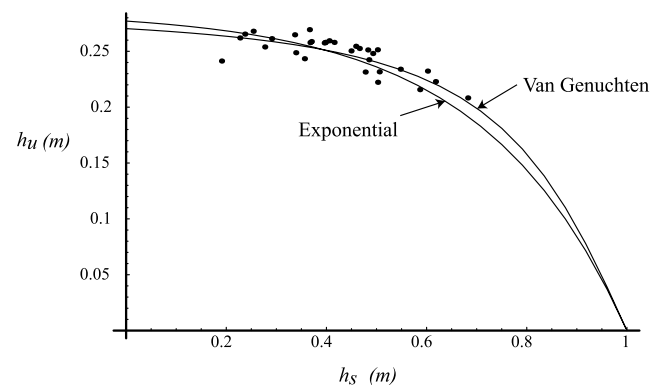


**Figure 9.** The saturated-unsaturated soil moisture storage for the spatially averaged Shale Hills data (dots) during the experiment. The solid lines represent the theoretical “steady state” saturated-unsaturated storage relationship for the shallow groundwater assumption based on the van Genuchten and the exponential soil characteristic. See section 6.5 for specific parameters. Note that  $h_s = h_g - z_b$  and the height of saturation above bedrock is plotted in this case, where  $z_b$  is the elevation of the shale bedrock.



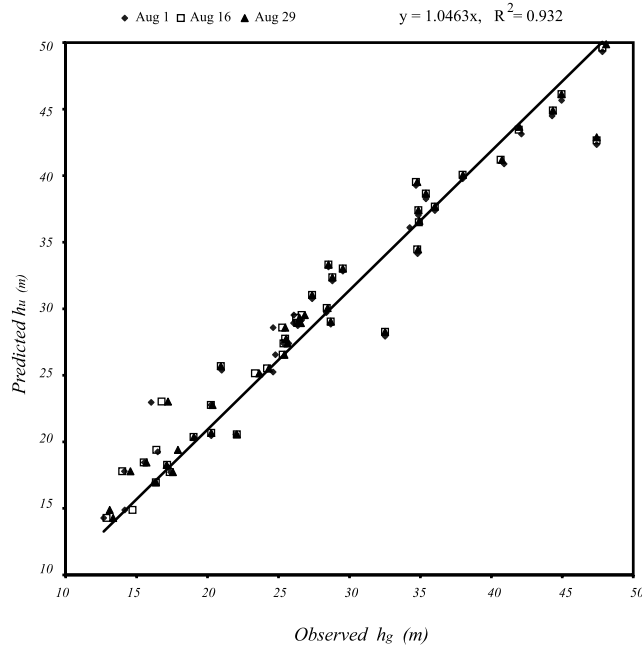


**Figure 10.** Observed and model groundwater levels for 1 August, 16 August, and 29 August. The fit is not significantly different from a slope of 1.

### 6.5. Simplified Shale Hills Model

[44] The system of equations developed in section 3 was used to model the Shale Hills site. However, it was determined that a simplification was possible as a result of the shallow soil at the site. *Duffy* [2004] developed a theoretical argument, that where the groundwater table is near the land surface, the governing equations for subsurface flow can be simplified into a single state by applying the “enslaving principal.” That is, the water table enslaves the soil moisture such that

$$\frac{dh_u}{dt} = G(h_g) \frac{dh_g}{dt} \quad (34)$$

$$G(h_g) = \frac{dh_u}{dh_g}, \quad (35)$$

where  $G(h_g)$  can be thought of as the integrated form of the soil characteristic function (see *Duffy* [2004] for details). This argument is essentially what was done by *Bierkens* [1998] in an earlier paper. The coupled two-state subsurface model (20) can now be reduced to

$$G(h_g) \frac{dh_g}{dt} = p + q^+ - et + \sum_{j=1}^3 q_j^g. \quad (36)$$

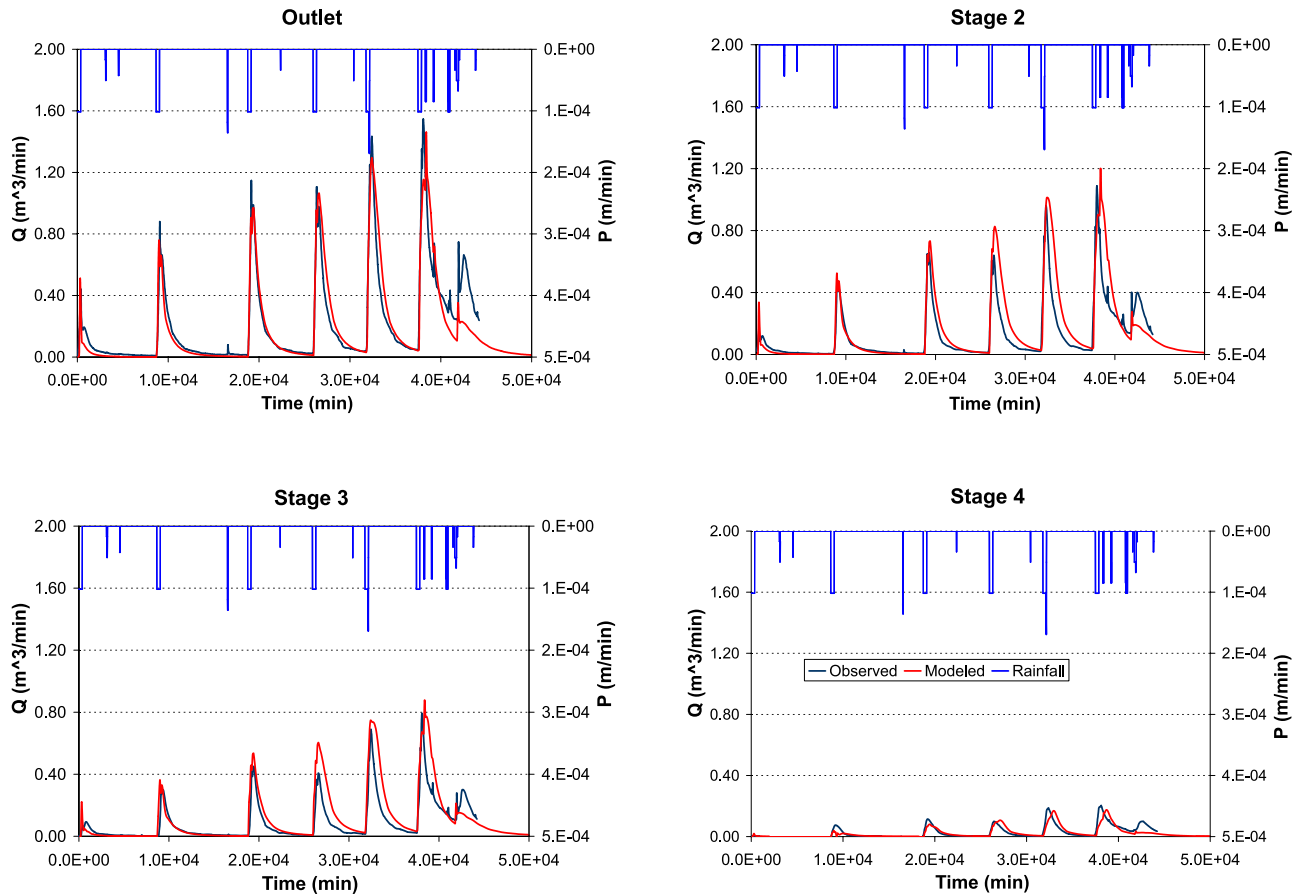


**Figure 11.** Observed (blue) versus model (red) runoff simulation for Shale Hills experiment. Note that the coupled model successfully simulates the internal runoff at each weir, including the upper ephemeral part of the channel.

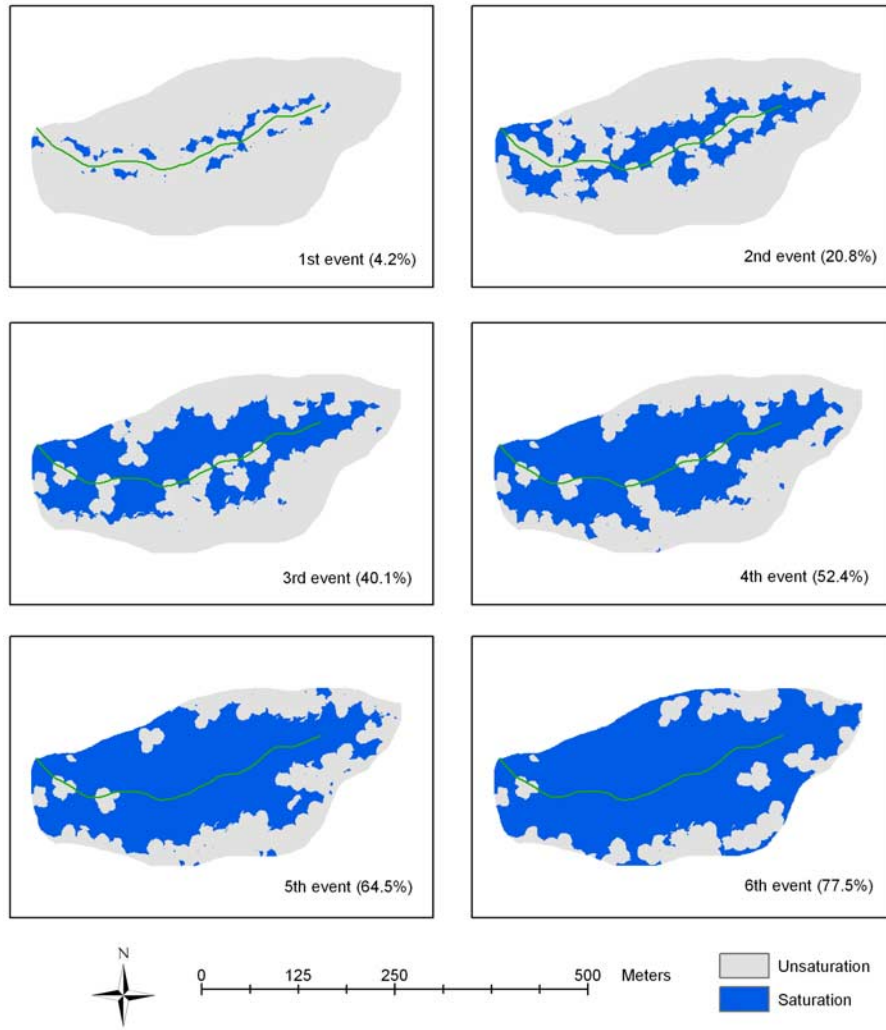


**Figure 12.** The simulated surface saturation area immediately after each of the six rainfall events. Note that the saturation area is patchy and unconnected after the first two events, with little connectivity to the channel. The patches of saturation occur at a local break in slope or within topographic depressions. For later events, the connectivity increases as the water table rises and saturation overland flow occurs. It is noted that the saturation values were interpolated to 1-m resolution using inverse distance weighting from the triangle elements.

Bierkens [1998] uses the van Genuchten soil characteristic function to derive a form for  $G(h_g)$  in (34) given by

$$G(h_g) = \varepsilon_0 + (\theta_s - \theta_r) \left( 1 - (1 + (\alpha(z_s - h_g))^n)^{-((n+1)/n)} \right), \quad (37)$$

where  $h_g$  and  $z_s$  are height of phreatic surface and surface elevation of the layer relative to some reference. The  $\varepsilon_0$  is a small parameter to handle the singularity in the function  $G(h_g)^{-1}$  when  $h_g \rightarrow z_s$ . The  $\theta_s$  and  $\theta_r$  are saturated and residual moisture content, and  $\alpha$  and  $n$  are soil parameters. Substituting (18) and (35) into (37), and performing the integration yields an expression for  $h_u$  as a function of  $h_g$ :

$$h_u = \frac{1}{\alpha} \left[ 1 + (\alpha(z_s - h_g))^n \right]^{-\frac{1}{n}}. \quad (38)$$

A similar expression can be developed for the exponential soil characteristic (22) shown earlier which is given by

$$h_u = \frac{1}{\alpha} \left( 1 - e^{-\alpha(z_s - h_g)} \right). \quad (39)$$

Using the site averaged data for  $h_u$  and  $h_g$ , the parameters in (38) and (39) were estimated and the results shown in Figure 9. The mean data from Figure 9 were used together with the soil survey information to estimate van Genuchten parameters used in the simulation:  $\theta_s = 0.40$ ,  $\theta_r = 0.05$ ,  $\alpha = 2.0 \text{ L/m}$ ,  $n = 1.8$ ,  $0.6 \leq z_s \leq 2.5 \text{ m}$ , and  $K_s = 1 \times 10^{-5} \text{ m/s}$ . Also note in Figure 9 that the height of saturation above the shale bedrock elevation is plotted using  $h_s = h_g - z_b$ .

## 6.6. Model Results

[45] For the domain, forcing, and a priori parameters described above, the simulation was carried out on a dual-processor desktop machine, completing the simulation in a

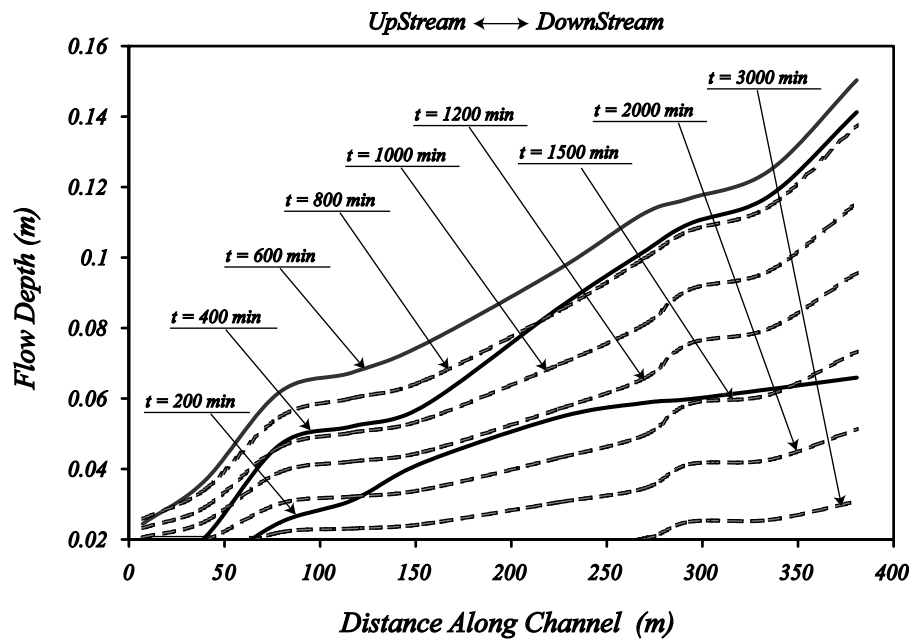


**Figure 13.** The flow depth along the channel for the third irrigation event. The solid lines show the distribution of flow depth during the event and immediately after the event (600 min). The dashed lines show the flow depth during the relaxation or recession period. The outlet weir is located on the right side of the graph.

few seconds. Because of the relatively small scale of the simulation, computational efficiency is not an issue in this problem. Figure 10 compares modeled and observed groundwater depth for three days during the experiment, 1 August, 16 August, and 30 August, respectively, with an overall regression slope of 1.05, and  $R = 0.965$ . Figure 11 illustrates simulated and observed runoff data at all four weirs. The first event does not match as well as others, due possibly to errors in the initial conditions, and this is discussed below. The sixth event also shows some departure, which might be related to our assumption to neglect canopy interception. It is interesting that both the observations and the model display a double peak in the hydrograph for each single rainfall event (Figure 11). This seems to be caused by a complex interaction of surface runoff controlled by small-scale topography and near-channel surface runoff, with subsurface flow. Additional experiments are necessary to partition the precise effects, but it is clear that the fully coupled distributed model can capture this kind of behavior. For the Shale Hills field experiment the rainfall-runoff generation mechanisms assumed in the model include Hortonian overland flow due to precipitation excess, and saturation overland flow. During most of the numerical experiment, the soil infiltration capacity is large enough to accommodate rainfall, and Hortonian flow is of limited importance except in the upland regions during the fifth and sixth events. Saturation overland flow occurs at locations where water table saturates the land surface from below. In Figure 12, the simulated regions of surface saturation after each rainfall event are plotted. Note that the saturation area is patchy and unconnected during the first two events with little connectivity to the channel. The patches of saturation occur at a local break in slope or in

topographic depressions. Recall that the hydraulic properties of the soil and the forcing in the watershed are homogeneous, and thus local variability is largely the result of topography. The impact of noncontiguous temporary patches of saturation is that the water reinfilters locally since it does not have a path to the channel. This threshold for surface flow due to local topography is discussed by *VanderKwaak and Loague* [2001], and they introduce a subgrid parameterization to resolve it.

[46] For later rainfall events (3–6), the connectivity of surface saturation increases as the water table rises and saturation overland flow connects the patches with the channel. Rejected rainfall during the later events also contributes to an increase in saturated area. In this analysis, the surface and bedrock topography exert a strong control on saturation overland flow, and thus have a dominant impact on surface runoff in Shale Hills experiment. This is similar to observations of *Amerman* [1965] and *Dunne and Black* [1970a, 1970b] at other northeastern watersheds.

[47] Another aspect of the simulation observed in Figure 11 is the onset of streamflow in the upper ephemeral channel reach. Channel flow in the upper part of the watershed is only observed during years with heavy snow or after very large fall storms. Figure 13 shows the integrated model result for flow depth along the channel in response to the third rainfall event. The beginning of the third rainfall is identified as 0 min and most of the channel is dry (not shown). During the event (200 min) the length of flowing channel has grown considerably. After 400 min the event is over, and the channel continues to grow until about 10 hours, when it reaches a maximum and begins to relax. After 3000 min the channel reach is largely dry again. The ability to examine the internal details of the flow is an

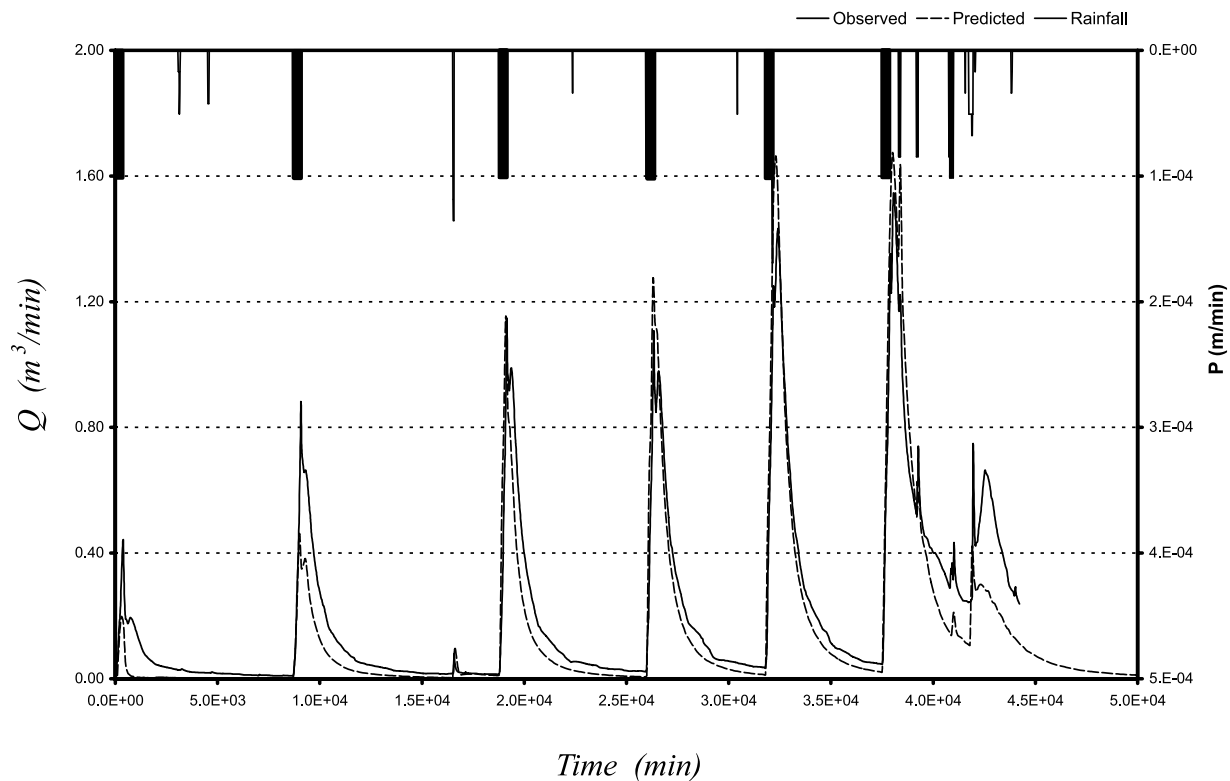


**Figure 14.** Simulation of the effect of a dry initial condition (drought persistence) on runoff at the outlet. The initial condition for soil moisture and groundwater level was set to very low values and then the experimental forcing was applied to the model. Note that the recovery is complete at approximately 333 hours.

important aspect of the fully coupled approach, including thresholds of wet and dry channels.

### 6.7. Sensitivity to Initial Conditions

[48] Next we simulate the impact of very dry antecedent soil moisture and low water table conditions to get some idea of the time it takes the watershed to recover from a major drought. The model is run with the same forcing sequence except that the initial states (groundwater and soil moisture) are reduced to the minimum possible values. The response at the outlet weir is shown in Figure 14. Note that it takes a relatively short time for a complete recovery of peak flow as compared with the previous simulation (third event or 333 hours). This simple result offers a clue that there is some problem with our assumptions in the model, since it has been subsequently observed during the 1990's drought, that the outlet weir completely dried up and did not recover for several years. This suggests that there might be a slower and deeper flow component (e.g., a multiyear timescale) within the underlying less permeable shale regolith. This might also explain the missing mass described earlier, and this study is currently under way.

## 7. Conclusions

[49] In this paper we describe a semidiscrete finite volume strategy for fully coupled integrated hydrologic model that is efficient for adding and subtracting processes and for constructing the discrete solution domain. We demonstrate

the strategy by coupling equations for a mixed PDE-ODE system that includes 2-D overland flow, 1-D channel flow, 1-D unsaturated flow, and 2-D groundwater flow, canopy interception, and snowmelt. The complete system of equations including constitutive or closure relations is coupled directly within a local kernel for a single prismatic element. GIS tools are used to decompose the domain into an unstructured grid, and the kernel is distributed over the grid and assembled to form the global ODE system. The global ODE system is solved with a state-of-the-art ODE solver. The strategy provides an efficient and flexible way to couple multiple distributed processes that can capture detailed dynamics with a minimum of elements. The FVM guarantees mass conservation during simulation at all cells. The model is referred to as the Penn State Integrated Hydrologic Model (PIHM).

[50] The approach has been implemented at the Shale Hills field experiment in central Pennsylvania. Model results show that it can successfully simulate observed groundwater levels, as well as runoff at the outlet and at internal points within the watershed using a priori parameters. The simulation is used to identify the important runoff generation mechanisms, and to illustrate the impact of antecedent soil moisture and groundwater level for amplifying the volume and peak runoff in the watershed. The effect of complex topography is shown to be a very important control on infiltration/reinfiltration areas within the watershed. The coupled model is able to simulate the



onset and relaxation of ephemeral streamflow in the upland part of the watershed. The processes and components of the model have been individually tested, and these results are given by Qu [2005]. A complete GIS interface for PIHM is currently being finalized for Web posting as a flexible and easily implemented open-source community modeling resource.

[51] **Acknowledgments.** This research was funded by grants from the National Science Foundation (Science and Technology Center for Sustainability of Water Resources in Semi-Arid Regions, NSF EAR 9876800; Integrated modeling of precipitation-recharge-runoff at the river basin scale: The Susquehanna, NSF ER030030), the National Oceanic and Atmospheric Administration (Modeling seasonal to decadal oscillations in closed basins, NOAA GAPP Program, NA04OAR4310085), and the National Aeronautics and Space Administration (The role of soil moisture and water table dynamics in ungaged runoff prediction in mountain-front systems, NASA—GAPP Program, ER020059). This support is kindly acknowledged.

## References

- Abbott, M. B., J. A. Bathurst, and P. E. Cunge (1986a), An introduction to the European Hydrological System—Système Hydrologique Européen “SHE”: part 1. History and philosophy of a physically based distributed modeling system, *J. Hydrol.*, **87**, 45–59.
- Abbott, M. B., J. A. Bathurst, and P. E. Cunge (1986b), An introduction to the European Hydrological System—Système Hydrologique Européen “SHE”: part 2. Structure of a physically based distributed modeling system, *J. Hydrol.*, **87**, 61–77.
- Allen, R. G., L. S. Pereira, D. Raes, and M. Smith (1998), Crop evapotranspiration, *FAO Irrig. Drain. Pap.* 56, United Nations Food and Agric. Organ., Rome.
- Amernman, C. R. (1965), The use of unit-source watershed data for runoff prediction, *Water Resour. Res.*, **1**(4), 499–508.
- Ascher, U. M., and L. R. Petzold (1998), *Computer Methods for Ordinary Differential Equations and Differential Algebraic Equations*, Soc. for Ind. and Appl. Math., Philadelphia, Pa.
- Beven, K. (2006), Searching for the holy grail of scientific hydrology:  $Q_t = H(SR)A$  as closure, *Hydrol. Earth Syst. Sci. Discuss.*, **3**, 769–792.
- Bierkens, M. F. P. (1998), Modeling water table fluctuations by means of a stochastic differential equation, *Water Resour. Res.*, **34**(10), 2485–2499.
- Brandes, D. (1998), A low-dimensional dynamical model of hillslope soil moisture, with application to a semiarid field site, Ph.D. thesis, Pa. State Univ., University Park.
- Bras, R. L. (1990), *Hydrology: An Introduction to Hydrologic Science*, Addison-Wesley, Boston, Mass.
- Brooks, R. H., and A. T. Corey (1964), Hydraulic properties of porous media, *Hydrol. Pap.* 3, Colo. State Univ., Fort Collins.
- Cohen, S. D., and A. C. Hindmarsh (1994), CVODE user guide, *Rep. UCRL-MA-118618*, Numer. Math. Group, Lawrence Livermore Natl. Lab., Livermore, Calif.
- Crawford, N. H., and R. K. Linsley (1966), Digital simulation on hydrology: Stanford Watershed Model IV, *Stanford Univ. Tech. Rep.* 39, Stanford Univ., Palo Alto, Calif.
- Delanunay, B. (1934), Sur la sphere vide, *Bull. Acad. Sci. USSR Class Sci. Math. Nat.*, **7**(6), 793–800.
- Dingman, S. L. (1994), *Physical Hydrology*, Prentice-Hall, Upper Saddle River, N. J.
- Du, Q., V. Faber, and M. Gunzburger (1999), Centroidal Voronoi tessellations: Applications and algorithms, *SIAM Rev.*, **41**(4), 637–676.
- Duffy, C. J. (1996), A two-state integral-balance model for soil moisture and groundwater dynamics in complex terrain, *Water Resour. Res.*, **32**(8), 2421–2434.
- Duffy, C. J. (2004), Semi-discrete dynamical model for mountain-front recharge and water balance estimation, Rio Grande of southern Colorado and New Mexico, in *Groundwater Recharge in a Desert Environment: The Southwestern United States*, *Water Sci. Appl. Ser.*, vol. 9, edited by J. F. Hogan et al., pp. 255–271, AGU, Washington, D. C.
- Dunne, T., and R. D. Black (1970a), An experimental investigation of runoff production in permeable soils, *Water Resour. Res.*, **6**(2), 478–490.
- Dunne, T., and R. D. Black (1970b), Partial area contributions to storm runoff in a small New England watershed, *Water Resour. Res.*, **6**(5), 1296–1311.
- Freeze, R. A., and R. L. Harlan (1969), Blueprint for a physically-based, digitally-simulated hydrologic response model, *J. Hydrol.*, **9**, 237–258.
- Gardner, W. R. (1958), Some steady-state solutions of the unsaturated moisture flow equation with application to evaporation from a water table, *Soil Sci.*, **85**, 228–232.
- Gottardi, G., and M. Venutelli (1993), A control-volume finite-element model for two-dimensional overland flow, *Adv. Water Resour.*, **16**, 277–284.
- Hauser, G. E. (2003), River modeling system user guide and technical reference, report, Tenn. Valley Auth., Norris, Tenn.
- Kristensen, K. J., and S. E. Jensen (1975), A model for estimating actual evapotranspiration from potential evapotranspiration, *Nord. Hydrol.*, **6**, 170–188.
- LaBolle, E. M., A. A. Ayman, and E. F. Graham (2003), Review of the integrated groundwater and surface-water model (IGSM), *Ground Water*, **41**(2), 238–246.
- Leveque, R. J. (2002), *Finite Volume Methods for Hyperbolic Problems*, Cambridge Univ. Press, New York.
- Lynch, J. A. (1976), Effects of antecedent moisture on storage hydrographs, Ph.D. thesis, 192 pp., Dep. of Forestry, Pa. State Univ., University Park.
- Lynch, J. A., and W. Corbett (1985), Source-area variability during peakflow, in watershed management in the 80's, *J. Irrig. Drain. Eng.*, 300–307.
- Madsen, N. K. (1975), The method of lines for the numerical solution of partial differential equations, in *Proceedings of the SIGNUM Meeting on Software for Partial Differential Equations*, pp. 5–7, ACM Press, New York.
- Maidment, D. R. (2002), *Arc Hydro: GIS for Water Resources*, 140 pp., ESRI Press, Redlands, Calif.
- Palacios-Velez, O. L., and B. Duevas-Renaud (1986), Automated river-course, ridge and basin delineation from digital elevation data, *J. Hydrol.*, **86**, 299–314.
- Palacios-Velez, O., W. Gandoy-Bernasconi, and B. Cuevas-Renaud (1998), Geometric analysis of surface runoff and the computation order of unit elements in distributed hydrological models, *J. Hydrol.*, **211**, 266–274.
- Panday, S., and P. S. Huyakorn (2004), A fully coupled physically-based spatially-distributed model for evaluating surface/subsurface flow, *Adv. Water Resour.*, **27**, 361–382.
- Polis, M. F., and D. M. McKeown (1993), Issues in iterative TIN generation to support large scale simulations, paper presented at 11th International Symposium on Computer Assisted Cartography (AUTOCARTO11), Minneapolis, Minn.
- Post, D. E., and L. G. Votta (2005), Computational science demands a new paradigm, *Phys. Today*, **58**(1), 35–41.
- Qu, Y. (2005), An integrated hydrologic model for multi-process simulation using semi-discrete finite volume approach, Ph.D. thesis, 136 pp., Civ. and Environ. Eng. Dep., Pa. State Univ., Univ. Park.
- Reggiani, P., and T. H. M. Rientjes (2005), Flux parameterization in the representative elementary watershed approach: Application to a natural basin, *Water Resour. Res.*, **41**, W04013, doi:10.1029/2004WR003693.
- Reggiani, P., M. Sivapalan, and M. Hassanizadeh (1998), A unifying framework for watershed thermodynamics: Balance equations for mass, momentum, energy and entropy, and the second law of thermodynamics, *Adv. Water Res.*, **22**, 367–398.
- Reggiani, P., M. Hassanizadeh, M. Sivapalan, and W. G. Gray (1999), A unifying framework for watershed thermodynamics: Constitutive relationships, *Adv. Water Res.*, **23**, 15–39.
- Shewchuk, J. R. (1997), Delaunay refinement mesh generation, Ph.D. thesis, Carnegie Mellon Univ., Pittsburgh, Pa.
- Sivapalan, M., C. Jothityangkoon, and M. Menabde (2002), Linearity and non-linearity of basin response as a function of scale: Discussion of alternative definitions, *Water Resour. Res.*, **38**(2), 1012, doi:10.1029/2001WR000482.
- Slattery, J. (1978), *Momentum, Energy, and Mass Transfer in Continua*, Krieger, Melbourne, Fla.
- Sleigh, P. A., P. H. Gaskell, M. Berzins, and N. G. Wright (1998), An unstructured finite-volume algorithm for predicting flow in rivers and estuaries, *Comput. Fluids*, **27**(4), 479–508.
- Tarboton, D. G., R. L. Bras, and I. Rodriguez-Iturbe (1991), On the extraction of channel networks from digital elevation data, *Hydrol. Processes*, **5**, 81–100.
- VanderKwaak, J. E., and K. Loague (2001), Hydrologic response simulations for the R-5 catchment with a comprehensive physics-based model, *Water Resour. Res.*, **37**(4), 999–1013.
- van Genuchten, M. T. (1980), A closed form equation for predicting the hydraulic conductivity of unsaturated soils, *Soil Sci. Soc. Am. J.*, **44**, 892–898.
- Vivoni, E. R., V. Y. Ivanov, R. L. Bras, and D. Entekhabi (2004), Generation of triangulated irregular networks based on hydrological similarity, *J. Hydrol. Eng.*, **9**(4), 288–302.

- Voronoi, G. (1907), Nouvelles applications des paramètres continus à la théorie des formes quadratiques, *J. Reine Angewandte Math.*, 133, 97–178.
- Yeh, G. T., H. P. Cheng, J. R. Cheng, H. C. Lin, and W. D. Martin (1998), A numerical model simulating water flow, contaminant and sediment transport in a watershed systems of 1-D stream-river network, 2-D overland regime, and 3-D subsurface media (WASH123D: Version 1.0), *Tech. Rep. CHL-98-19*, U. S. Environ. Prot. Agency Environ. Res. Lab., Athens, Ga.
- 
- C. Duffy and Y. Qu, Department of Civil and Environmental Engineering, Pennsylvania State University, 212 Sackett Building, University Park, PA 16802, USA. (cxd11@psu.edu)